25-hydroxycholesterol dysregulates brain endothelial cell function and exacerbates cerebral haemorrhage

Victor S. Tapia[1,2,3], Sarah E. Withers[1,2,4], Ran Zhou[1,2], Abigail Bennington[2,5], Frances Hedley[1,2], Adam El Khouja[1,2], Nadim Luka[1,2], Marco Massimo[6,7], Siobhan Crilly[1,2], Katherine R. Long[6,7], Catherine B. Lawrence[1,2], and Paul R. Kasher*[1,2,3].

[1]Division of Neuroscience, School of Biological Sciences, Faculty of Biology, Medicine and Health, Manchester Academic Health Science Centre, The University of Manchester, Manchester, United Kingdom.

[2]Geoffrey Jefferson Brain Research Centre, The Manchester Academic Health Science Centre, Northern Care Alliance National Health Service (NHS) Foundation Trust, The University of Manchester, Manchester, United Kingdom.

[3]Lydia Becker Institute of Immunology and Inflammation, Faculty of Biology, Medicine and Health, Manchester Academic Health Science Centre, The University of Manchester, Manchester, UK

[4]Immunology and Inflammation Theme, Translational and Clinical Research Institute, Newcastle University, Newcastle, United Kingdom

[5]Division of Cardiovascular Sciences, School of Medical Sciences, Faculty of Medicine, Biology and Health, The University of Manchester, Manchester, UK

[6]Centre for Developmental Neurobiology, Institute of Psychiatry, Psychology and Neuroscience, King's College London, London, United Kingdom.

[7]MRC Centre for Neurodevelopmental Disorders, King's College London, London, United Kingdom.

* Corresponding author. Email: paul.kasher@manchester.ac.uk

Keywords: 25HC, cholesterol, intracerebral haemorrhage

Abstract

Viral infection and hypocholesterolaemia are two independent risk factors for intracerebral haemorrhage (ICH), but the molecular mechanisms leading to vascular rupture via these risk factors remain unknown. We hypothesised that the enzyme cholesterol 25-hydroxylase (CH25H) and its metabolite 25-hydroxycholesterol (25HC), which modulates cholesterol metabolism during infection, may offer a mechanistic link between cholesterol dysregulation and infection during neurovascular dysfunction. We identified an upregulation of CH25H in infection-associated cerebral haemorrhage, in a SARS-CoV-2-induced zebrafish ICH model and foetal human SARS-CoV-2-associated cortical microbleeds. Using human brain endothelial cells and zebrafish ICH models, we show that 25HC promotes endothelial dysfunction and exacerbates brain bleeding. These effects involved cholesterol metabolism modulation, as cholesterol supplementation rescued these effects, while 25HC and statin treatments interacted to exacerbate dysfunction. We propose that the CH25H/25HC pathway represents an important component in the pathophysiology of brain vessel dysfunction associated with infection and cholesterol dysregulation in the context of ICH.

Introduction

Intracerebral haemorrhage (ICH) is the second most common type of stroke and a leading global health burden [1]. While several ICH risk factors have been described [1,2], how they lead to cerebrovascular dysfunction and brain vessel rupture is not completely understood. Acute and chronic viral infections such as SARS-CoV-2, varicella, herpes and hepatitis C have been proposed to increase ICH risk [3-6]. Alongside adult ICH, SARS-CoV-2 infections have also been associated with foetal brain haemorrhages [7]. Viral infections may be a direct trigger of brain vessel rupture, as within 24 hours of fever and flu-like symptoms the risk of ICH increases [8]. Insight into how viral infection leads to brain vessel dysfunction will improve the understanding of ICH pathophysiology.

While ICH shares several modifiable risk factors with ischaemic stroke [1], including viral infections already mentioned [4-6], the contrasting role of circulating cholesterol levels presents a striking difference between the two forms of stroke. Hypocholesterolaemia has been described as a clinical risk factor for ICH [9-11], in opposition to the well-established link between high cholesterol levels and ischaemic stroke [1]. Pharmacological inhibition of cholesterol synthesis using statins, a common treatment for high blood cholesterol-related cardiovascular disease, has also been debated as an ICH risk factor [12,13]. How hypocholesterolaemia is associated with ICH is not understood. In a retrospective longitudinal study, a decline in total cholesterol and low-density lipoprotein cholesterol (LDL-C) levels was observed in ICH patients during the 6 months prior to haemorrhage [11]. This temporal association suggests other biological factors may exist to induce hypocholesterolaemia and ultimately increase ICH risk.

While infection and hypocholesterolaemia have not been associated together as ICH risk factors, an interesting link between viral infection and a reduction in cholesterol levels has been established through the type I interferon (IFN) pathway. Clinical studies using IFN as an antiviral treatment have reported a decrease in blood cholesterol levels [14]. At a cellular level, IFN signalling decreases cholesterol availability to protect cells against viral entry and replication. This is mediated by the upregulation of the IFN-stimulated enzyme cholesterol 25-hydroxylase (CH25H) and its metabolite 25-hydroxycholesterol (25HC) [15]. The antiviral mechanisms of 25HC have been well described, involving the decrease of plasma membrane cholesterol availability and inhibition of cholesterol synthesis [15-17]. Besides their role in immune defence, recent studies have shown that the CH25H/25HC pathway has a detrimental role in vascular function in certain pathologies, such as atherosclerosis, lung inflammation and experimental autoimmune encephalomyelitis (EAE) [18-20]. Considering both viral infection and hypocholesterolaemia as ICH risk factors, we therefore hypothesize that the CH25H/25HC pathway could play a role in the development of ICH.

Using a zebrafish model of statin-induced brain bleeding [21], we recently described an Aicardi-Goutières syndrome model that links IFN signalling, cholesterol dysregulation, and susceptibility to ICH [22]. In this present study, we expand on this work and evaluate the effect of the antiviral CH25H/25HC pathway on cholesterol dysregulation and brain endothelial dysfunction. Initially, we characterized the upregulation of CH25H in SARS-CoV-2-injected zebrafish larvae and human SARS-CoV-2-associated developmental brain haemorrhages. Subsequently, we evaluated the effects of 25HC on hCMEC/D3 cells, a human brain endothelial cell (EC) line, and zebrafish ICH models. Overall, we found that 25HC induces dysregulation of cholesterol metabolism and brain EC function. Dysregulation of EC function was dependent on cholesterol metabolism, as cell function was rescued by cholesterol supplementation and worsened by pharmacological inhibition by statins. 25HC also increased the severity of statin-induced ICH in zebrafish larvae. We propose that induction of the CH25H/25HC pathway could be an important pathway in infection-triggered brain EC dysfunction, offering a mechanistic link between infection and cholesterol dysregulation in ICH events.

Results

CH25H is expressed in infection-associated developmental intracerebral haemorrhage

To evaluate the role of CH25H/25HC in brain vascular dysfunction, first we aimed to evaluate the expression of CH25H in infection-associated ICH. For this, we took advantage of a SARS-CoV-2 infection model in zebrafish larvae. Injection of the SARS-CoV-2 spike protein (spike) into the hindbrain of zebrafish larvae induced an inflammatory response and brain haemorrhages [23]. To confirm these findings, we used a zebrafish double transgenic reporter for endothelial cells and erythrocytes (Tg(fli1:EGFP)/Tg(gata1a:DsRed)) to evaluate spike-induced brain haemorrhages *in vivo* (Fig. 1A). Spike injections were compared to non-injected, BSA or denatured (80ºC, 30 min) spike protein (spike-80) injected control groups. Spike injection did not change brain haemorrhage frequency at 3 or 8 hours post-injection but induced a significant increase in frequency at 24 hours (Fig. 1B). Furthermore, a significant increase in brain haematoma area was also observed at 24 hours post-injection in spike-injected larvae compared to BSA controls (Fig. 1C). We then evaluated the expression of the five *CH25H* homolog genes described in zebrafish [24]. *Ch25h* was transiently upregulated by spike injection before the increase in brain haemorrhage frequency, as observed by a significant upregulation at 8 hours post-injection and return to basal levels at 14 hours (Fig. 1D). In contrast, spike injection had no effect on the other zebrafish homolog genes *ch25hl1.1*, *ch25hl2* and *ch25hl3* (Fig. 1E) and *ch25hl1.2* was not detected (not shown). These findings corroborate previous research indicating that zebrafish *ch25h* is upregulated in response to viral challenge, whereas the other *ch25h* homologs do not exhibit the same antiviral upregulation [24].

To translate these findings, we used post-mortem human foetal brain samples where SARS-CoV-2 infection was found to be associated with cortical microbleeds [7]. First, we quantified microbleed number and size in the cortical samples, observing a variable size of microbleed which we classified in three area size categories (Fig 2A). Measuring the number and size of microbleeds, we classified the cortical samples by a bleeding score, where non-haemorrhagic samples had a score 0, and haemorrhagic samples were divided into scores 1 and 2. Score 2 samples had significantly more bleeds, quantified by total density number (Fig. 2B), and significantly more bleeds of medium size (Fig. 2C). We then evaluated CH25H levels by immunohistochemistry, observing a lack of CH25H+ cells in non-haemorrhagic samples and variable numbers of CH25H+ cells in haemorrhagic samples (Fig. 2D). A significant increase in CH25H+ cells was observed in samples with a bleeding score of 2 (Fig. 2E). Next, we analysed the distribution of CH25H+ cells, as they were found both proximal and distal to microbleeds (Fig. 2D). CH25H+ cells were located up to 2500 µm away from haemorrhagic cores, located further away from microbleeds in samples from score 2 (Fig. 2F). We then evaluated whether CH25H expression was linked to local infection, as the original study detected SARS-CoV-2 spike protein not only in cortical tissue, but also in foetal choroid plexus and maternal tissue [7]. Using data collected in this previous study, we observed that spike protein levels in the same cortical samples did not correlate with bleeding score (Fig. 2G). This suggests that microbleeds and CH25H expression are not associated with local infection. Altogether, our data shows that CH25H upregulation is part of an antiviral response in SARS-CoV-2-associated haemorrhages in developing zebrafish and human brain.

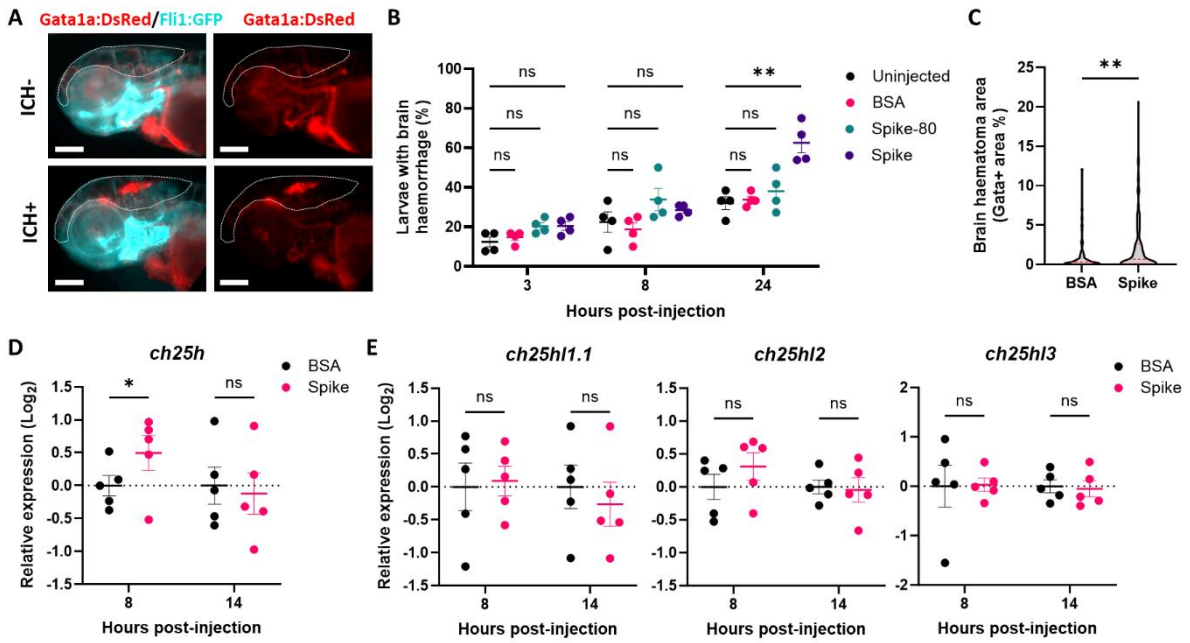

Figure 1. SARS-CoV-2 spike protein induces *ch25h* upregulation prior to spontaneous brain bleeding in zebrafish larvae. A Representative images of control (ICH-) and haemorrhagic (ICH+) *Tg(fli1:EGFP)/Tg(gata1a:DsRed)* 3 days post-fertilization (dpf) larvae, 24 hours after SARS-CoV-2 spike protein (spike) injection into the hindbrain (0.25 mg/ml, 2 nl). Red indicates erythrocytes (gata1a positive) and cyan endothelial cells (fli1+ positive). Dotted lines indicate brain area. Scale bars 250 µm. **B** Time course of ICH+ frequency in *Tg(fli:EGFP)/Tg(gata1a:DsRed)* larvae in uninjected, injected with BSA control, injected with pre-heated spike at 80 °C for 30 min (spike-80) or injected with spike conditions (n=4, 11-14 embryos per experiment). **C** Haematoma size (gata positive area in brain region) in larvae 24 h post-injection of BSA or spike (n=146-147 embryos, 3 independent experiments). **D-E** Gene expression was analysed in larval heads 8 and 14 hours after BSA or spike injections, for *ch25h* (**D**), *ch25hl1.1*, *ch25hl2* and *ch25hl3* (**E**). Data are mean ± S.E.M (**B**, **C**, **E**) or median ± quartiles (**C**). *, $p < 0.05$; **, $p < 0.01$; ns, non-significant, determined by repeated measures ANOVA with Dunnet's post-hoc test compared to uninjected (**B**), Mann-Whitney test (**C**), or randomized block two-way ANOVA with Sidak's post hoc analysis compared to BSA (**D, E**).

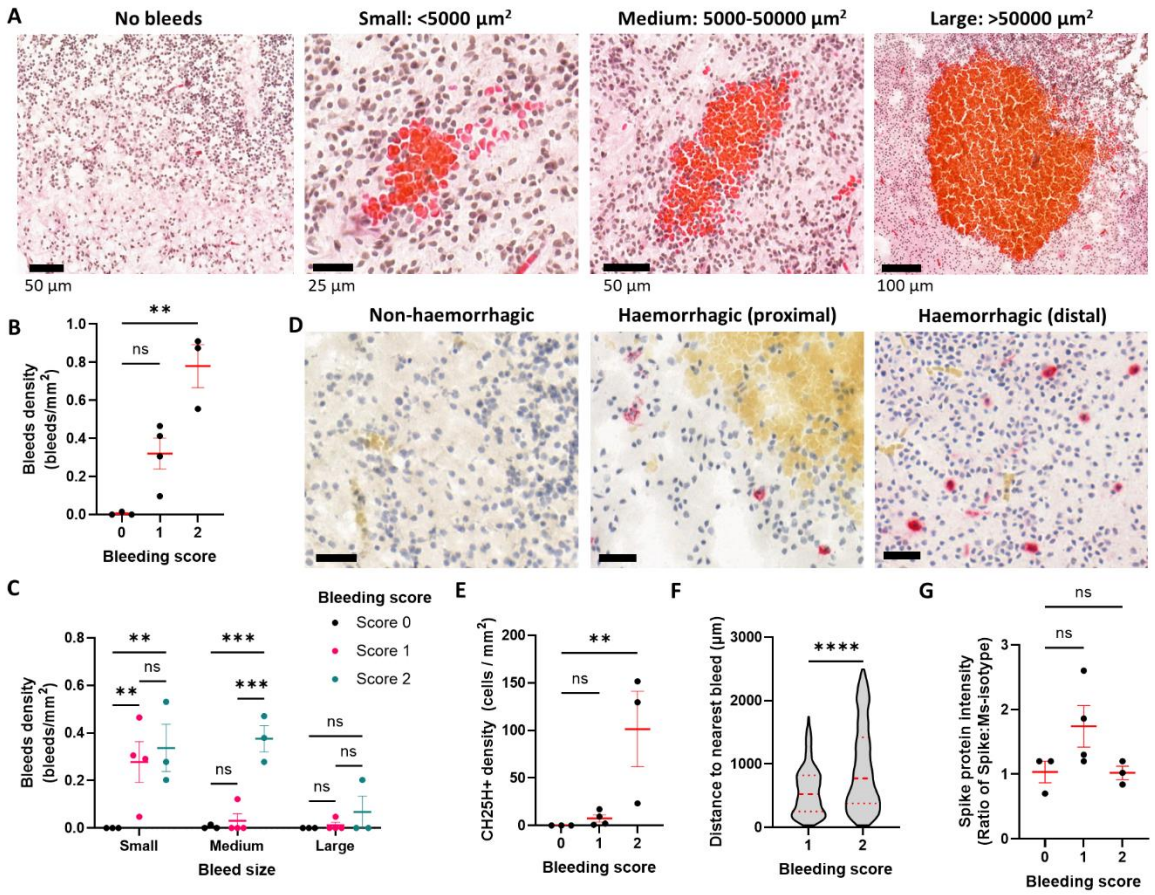

Figure 2. CH25H expression is associated with human foetal SARS-CoV-2-associated brain microbleeds. A Representative images of microbleeds found in human foetal cortex by H&E staining. Bleeds were classified into small, medium and large sizes according to area. Scale bar size is shown in each image. **B** Samples were categorised according to a bleeding score, based on bleed density. Control samples were classified in score 0, and haemorrhagic samples were classified in scores 1 and 2. **C** Density of small, medium, and large bleeds in samples with bleeding scores 0 to 2. **D** Representative images for CH25H staining (pink) and bleeds (yellow) from non-haemorrhagic or haemorrhagic samples, proximal and distal to bleeds. Scale bars 30 µm. **E** CH25H+ cell density was quantified in samples with bleeding scores 0 to 2. **F** Distance of CH25H+ cells to the nearest bleed was quantified in samples with bleeding scores 1 and 2 (n=626-702 cells). **G** Ratio of immunofluorescence integrated density of the SARS-CoV-2 spike protein relative to its isotype control, data obtained from [7], in samples with bleeding scores 0 to 2. Data are mean ± S.E.M (**B**, **C**, **E**, **F**) or median ± quartiles (**G**). **, $p < 0.01$; ***, $p < 0.001$; ***, $p < 0.0001$; ns, nonsignificant, determined by one-way ANOVA with Kruskal-Wallis post hoc test compared to score 0 (**B**, **E, G**), or two-way ANOVA with Tukey's post hoc analysis multiple comparisons between scores (**C**), or Mann-Whitney test (**F**).

25HC remodels cholesterol metabolism in human brain endothelial cells

We next aimed to evaluate the role of 25HC in brain EC function. As 25HC is secreted from cells and exerts a paracrine antimicrobial effect [15,25], we used the human brain EC line hCMEC/D3 as a model to evaluate the effects of 25HC exposure in brain ECs. Depletion of plasma membrane accessible cholesterol levels is one of the main antimicrobial mechanisms induced by 25HC [16,17,26]. Using Streptolysin O (SLO), a cholesterol-dependent cytolysin which binds to accessible cholesterol to form membrane pores [26], we indirectly evaluated accessible cholesterol levels by measuring cell permeability through uptake of the small dye ToPro3 (Fig. 3A). Following SLO pore formation, the percentage of permeable cells increased significantly from 3.6% to 89.0% under baseline conditions (Fig. 3B). This permeability was inhibited by 25HC pre-treatment in a concentration dependent manner (24 hours pre-treatment, 0.2 to 25 µM) (Fig. 3B), suggesting a reduction in accessible cholesterol levels. The highest concentration of 25HC, 25 µM, induced basal cell permeability (Fig. 3B). This is a sign of toxicity; therefore, we limited subsequent 25HC treatments to 5 µM. This concentration of 25HC did not induce apoptosis as measured by caspase-3 cleavage (Fig. 3C) and did not affect cell density (Fig. 3D), confirming that the viability of hCMEC/D3 cells was not affected by this condition.

We next evaluated the timing of cholesterol dysregulation. A time course analysis showed that depletion of accessible cholesterol was quickly induced, as inhibition of permeability reached 50% following 6 hours of 25HC (5 µM) exposure and continued to decrease through the 24 hours treatment (Fig. 3E). 25HC also remodels cholesterol metabolism by inhibition of SREBP2 (Sterol regulatory element-binding protein 2) and activation of LXR (Liver X receptor) transcription factors [16,27]. Four hours after 25HC exposure the expression of cholesterol synthesis enzymes *HMGCR* and *SQLE*, transcriptional targets of SREBP2 [27], was decreased in hCMEC/D3 cells (Fig. 3F). This treatment also upregulated *ABCG1* (Fig. 3G), an LXR target involved in cholesterol efflux [28]. Altogether, these results suggest that 25HC quickly remodels cholesterol metabolism in brain endothelial cells by decreasing accessible cholesterol levels, inhibiting cholesterol synthesis, and modulating cholesterol efflux.

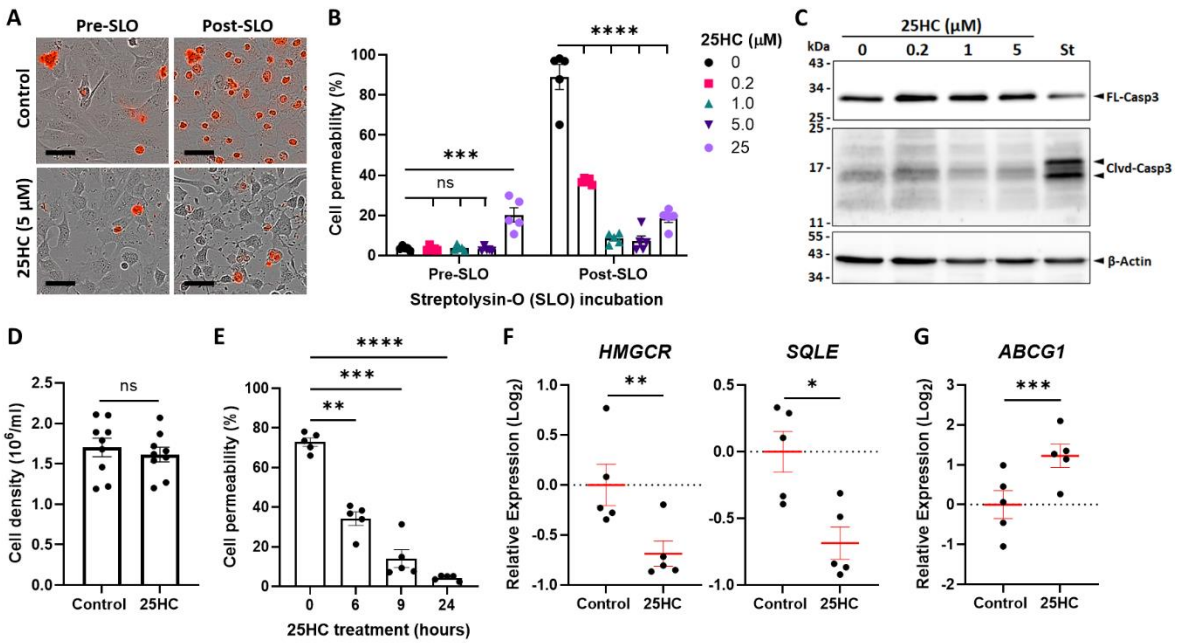

Figure 3. 25HC remodels cholesterol metabolism in human brain endothelial cells. A-B hCMEC/D3 cells were pre-treated with 25HC (0-25 µM, 24 h) before incubation with streptolysin O (SLO). Membrane permeability was measured by ToPro3+ uptake (red signal) before and after SLO, representative images (**A**) and quantification (**B**) are shown. Scale bars 37.5 µm. **C** Western blot analysis of hCMEC/D3 cell lysates pre-treated with 25HC (0-5 µM, 24 h), compared to staurosporine 5 µM (St) as apoptosis-positive control. Blots for full caspase-3 (FL-Casp3), activated cleaved caspase-3 (Clvd-Casp3) and β-actin as loading control, image is representative of three independent experiments. **D** hCMEC/D3 cell density after treatment with 25HC (5 µM, 24 h), counted using a haematocytometer after trypsin detachment. **E** Permeability of hCMEC/D3 cells, pre-treated with 25HC (5 µM) at different times, after streptolysin O (SLO) incubation was measured by ToPro3+ uptake. **F-G** Gene expression of *HMGCR, SQLE* (**F**), and *ABCG1* (**G**) in hCMEC/D3 cells after 25HC treatment (5 µM, 4 h). Data are mean ± S.E.M. **, $p < 0.01$; ***, $p < 0.001$; ****, $p < 0.0001$; ns, nonsignificant, determined by repeated measures two-way ANOVA with Sidak's post hoc test compared to 0 µM (**B**), paired t-test (**D**, **F**, **G**), or randomized block one-way ANOVA with Dunnet's post hoc test compared to 0 µM (**E**).

25HC disrupts the function of human brain endothelial cells

Cholesterol metabolism has been shown to regulate barrier function and EC migration [29,30]. As we characterized cholesterol metabolism changes induced by 25HC, we next questioned whether the function of hCMEC/D3 cells would also be affected. We analysed the permeability of fluorescein dextran 70 kDa (FD70) to evaluate endothelial barrier formation, a technique previously used to assess hCMEC/D3 barrier function [31]. 25HC induced a concentration dependent decrease of barrier function, with 25HC 5 µM treatment leading to a significant 85% increase in FD70 permeability (Fig. 4A). We next evaluated the collective migration of hCMEC/D3 cells by a previously established scratch assay [32] (Fig. 4B). One day pre-treatment with 25HC decreased cell migration in a concentration dependent manner (Fig. 4C). This effect was independent of proliferation, as cell cycle arrest using mitomycin C had no effect on cell migration inhibition (Fig. 4D) and as previously assessed, 25HC did not affect cell density (Fig. 3D).

Barrier function and EC migration are dynamically controlled by adherens junctions [33,34]. VE-cadherin is a key component of endothelial adherens junctions that are partially localised in cholesterol-enriched lipid rafts [35,36] and are sensitive to changes in cholesterol content [30,36]. Therefore, we next analysed the effects of 25HC on VE-cadherin distribution by immunofluorescence (Fig. 4E) and, using the Junction Mapper tool [37], we detected a significant increase in VE-cadherin intensity in cell junctions (Fig. 4F). This was not due to changes in total VE-cadherin levels, as total levels analysed from hCMEC/D3 cell lysates were not significantly affected by 25HC (Fig. 4G-H). The impairment in barrier function and cell migration suggests that VE-cadherin accumulation in cell-to-cell junctions is dysfunctional, which could be related to the association between plasma membrane cholesterol and VE-cadherin function.

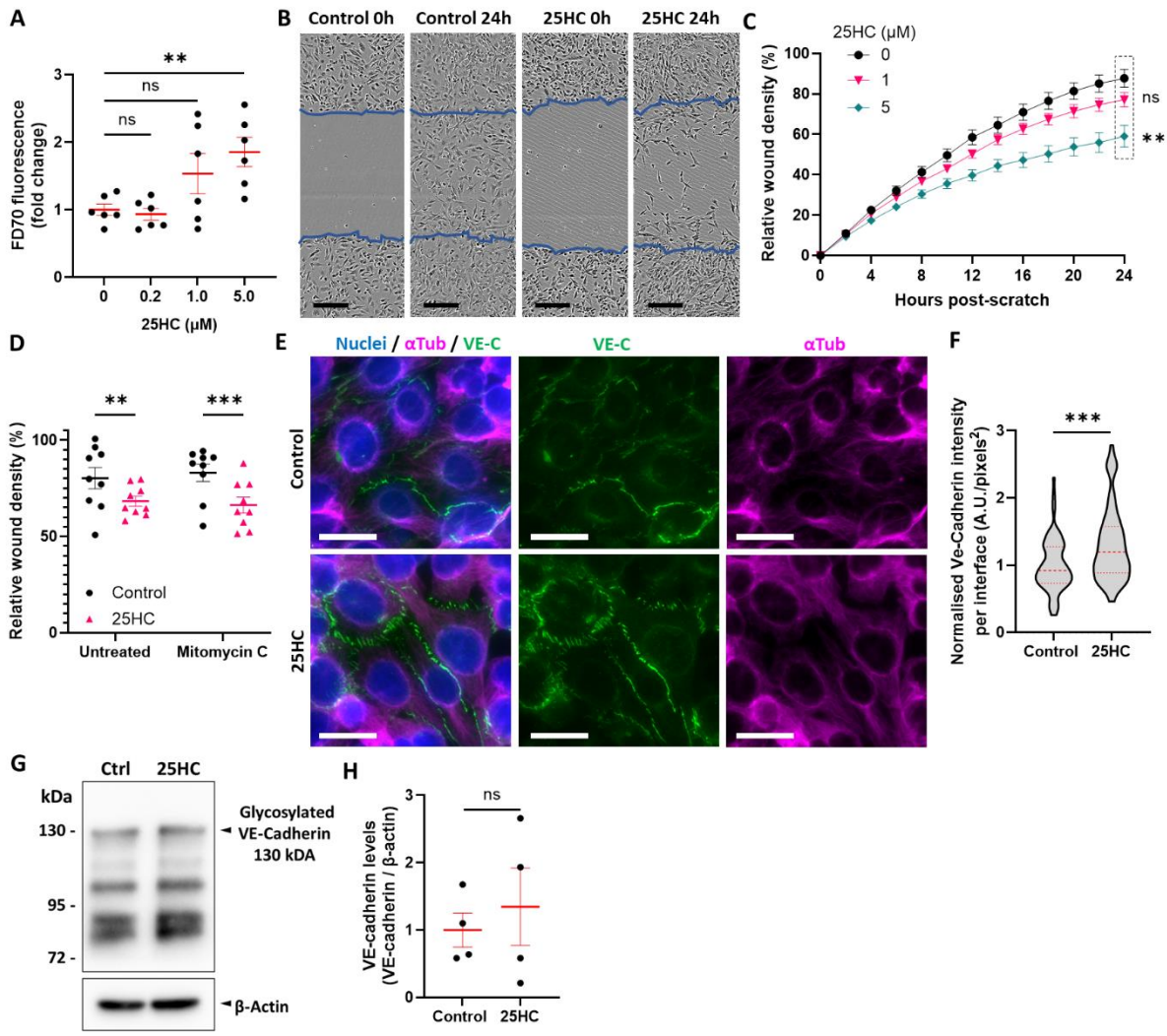

Figure 4. 25HC dysregulates the function of human brain endothelial cells. A Permeability of fluorescein-conjugated dextran 70 kDa (FD70) in hCMEC/D3 cell monolayer pre-treated with different concentrations of 25HC (0-5 µM, 24h). **B-C** hCMEC/D3 cell migration in a scratch assay, cells were pre-treated with different concentrations of 25HC (0-5 µM, 24 h before scratch). Representative images are shown for cells 0 and 24 hours after scratch (**B**, 25HC 5 µM). Blue lines show initial scratched area. Scale bars 100 µM. Migration was quantified as relative wound density (**C**, n=10). **D** hCMEC/D3 cell migration 24 hours post-scratch, pre-treated with 25HC (5 µM, 24 h before scratch) and then mitomycin D (5 µg/ml, 2 h before scratch). **E-F** Representative immunofluorescence (**E**) images of VE-cadherin (green), αTubulin (magenta) and nuclei (blue) in control and 25HC-treated (5 µM, 24 h) hCMEC/D3 cells. Scale bars 25 µm. VE-cadherin intensity in cell junctions (**F**) was analysed by junction mapper tool in control and 25HC-treated hCMEC/D3 cells (n=73-76 cells, 5 independent experiments). **G-H** VE-cadherin protein levels and β-actin as loading control were analysed by Western Blot in hCMEC/D3 after 25HC treatment (5 µM, 24h). Representative image (**G**) and densitometry analysis of 130 kDa VE-cadherin (**H**, n=4). Data are mean ± S.E.M (**A**, **C**, **D**, **H**) or median ± quartiles (**F**). **, $p < 0.01$; ***, $p < 0.001$; ns, nonsignificant, determined by randomized block one-way ANOVA with Dunnet's post-hoc test compared to 0 µM (**A**), matched measures two-wat ANOVA with Dunnet's post-hoc test compared to 0 µM (**C**), randomized block two-way ANOVA with Sidak's post-hoc test compared to control group, Mann-Whitney U test (**F**) or paired t-test (**H**).

25HC-induced dysregulation of human brain endothelial cells depends on cholesterol metabolism

We next aimed to determine if cholesterol metabolism was involved in the 25HC-induced dysfunction of hCMEC/D3 cells. Cholesterol supplementation after 25HC treatment can rescue the decrease in accessible cholesterol levels and its associated microbial protection [17]. In our model, cholesterol supplementation (80 µM, 1 h) rescued the SLO-induced permeability phenotype (Fig. 5A), confirming that inhibition of cell permeability was due to a decrease in cholesterol levels. Next, we evaluated the role of cholesterol availability in barrier function. hCMEC/D3 cells were pre-treated with 25HC and then supplemented with soluble cholesterol. Six hours later FD70 permeability was evaluated, and we observed that cholesterol supplementation rescued the effect of 25HC on barrier function (Fig. 5B). Similarly, cholesterol supplementation also rescued 25HC inhibition of cell migration. hCMEC-D3 cells were pretreated with 25HC for 1 day and, before the scratch, supplemented with cholesterol for 2 hours. Cholesterol supplementation increased cell migration of 25HC-pretreated cells 12 and 24 hours post-scratch, while having no effect on control cells (Fig. 5C).

Pharmacological inhibition was used as a second approach to evaluate the role of cholesterol metabolism in 25HC-induced dysfunction. We used ATV to inhibit HMGCR, a key enzyme in the cholesterol synthesis pathway, which has been shown to disrupt EC barrier function at micromolar concentrations [38]. As 25HC decreased *HMGCR* expression in hCMEC/D3 cells (Fig. 3F), we hypothesised that ATV would exacerbate 25HC-induced cholesterol dysregulation. ATV treatment alone (1 µM, 24 h) had no effect on barrier function, while ATV and 25HC co-treatment significantly increased permeability in comparison to 25HC alone (Fig. 5D). A similar interaction between 25HC and ATV was observed in the scratch assay. ATV alone had no effect on cell migration, while it significantly exacerbated inhibition of cell migration in 25HC pre-treated cells 24 hours post-scratch (Fig. 5E). Altogether, both cholesterol supplementation and ATV pharmacological inhibition shows that the 25HC-induced dysfunction of brain ECs is dependent on cholesterol metabolism.

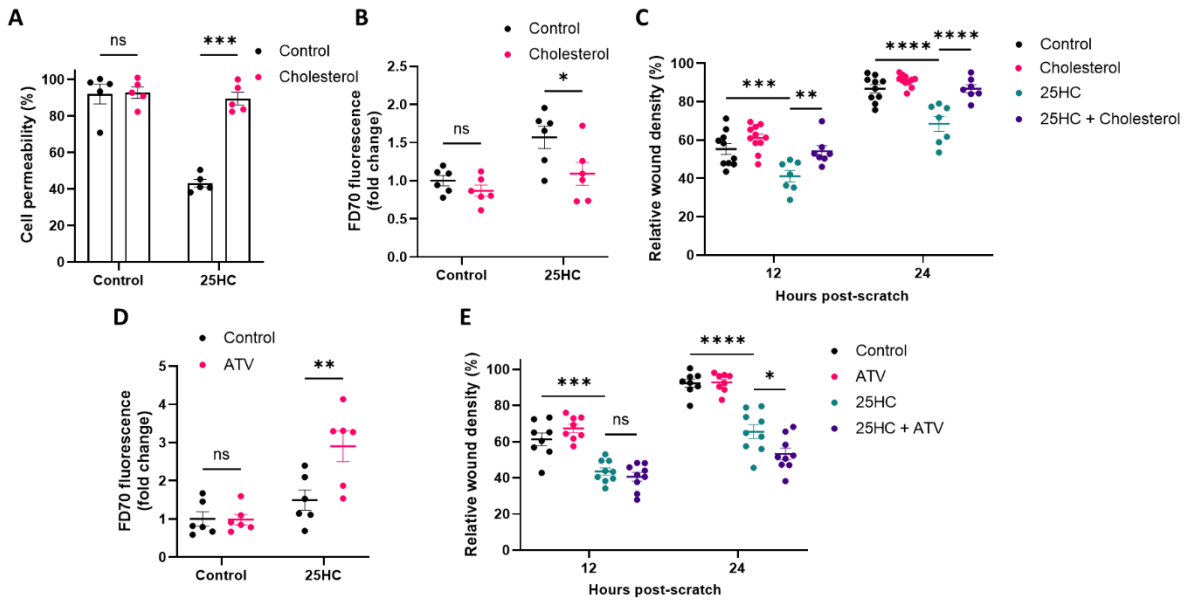

Figure 5. 25HC dysregulation of human brain endothelial cells depends on cholesterol metabolism. **A** Permeability of hCMEC/D3 cells, pre-treated with 25HC (5 µM, 6 h) and then with soluble cholesterol (80 µM, 1 h), after streptolysin O (SLO) incubation. **B** Fluorescein-conjugated dextran 70 kDa (FD70) permeability was analysed in hCMEC/D3 cells pre-treated with 25HC (5 µM, 14h) and then supplemented with soluble cholesterol (80 µM, 1h). **C** Cell migration at 12- and 24-hours post-scratch of hCMEC/D3 cells pre-treated with 25HC (5 µM, 24 h) and then supplemented with cholesterol (80 µM, 2 h) before scratch. **D** FD70 permeability was analysed in hCMEC/D3 cells treated with 25HC (5 µM, 24 h) and ATV (1 µM, 24 h). **E** Cell migration at 12- and 24-hours post-scratch of hCMEC/D3 cells pre-treated with 25HC (5 µM, 24h) before scratch and treated with ATV (1 µM, 24h) after scratch. Data are mean ± S.E.M. *, $p < 0.05$; **, $p < 0.01$; ***, $p < 0.001$; ****, $p < 0.0001$; ns, nonsignificant, determined by randomized block two-way ANOVA with Sidak's post-hoc test compared to control (**A**, **B**, **D**) or repeated measures two-way ANOVA with Tukey's post-hoc test and multiple comparisons (**C**, **E**).

25HC increases severity of bleeding in a statin-dependent zebrafish ICH model

Our *in vitro* brain EC observations suggested that cholesterol metabolism-dependent 25HC dysregulation could lead to impairment of the neuro-vasculature. To test this *in vivo*, we utilised the ATV-inducible zebrafish larval model of ICH. Pharmacological inhibition of HMGCR by statins induces spontaneous brain bleeding at 2 days post fertilization (dpf) in zebrafish larvae [21,22,38]. As we previously observed that ATV exacerbated 25HC-induced brain EC dysfunction (Fig. 5D-E), we hypothesised that 25HC would also worsen ATV-induced brain bleeding in zebrafish.

To test this, first, we confirmed that SRBEP2 inhibition by 25HC is a conserved process between zebrafish and mammals. Wild type (WT) zebrafish larvae that were incubated with 25HC (25 µM, 24 h) exhibited significantly reduced transcription of *hmgcrb* and *sqlea* (Fig. 6A), as previously observed in the orthologous human genes in the HCMEC/D3 model (Fig. 3F). To evaluate the effects of 25HC and ATV on brain bleeding in zebrafish, ATV-induced haemorrhages were identified by O-dianisidine staining (Fig. 6B) [22]. Following ATV incubation, 25HC was injected (1 nl, 5 µM) directly into the bloodstream through the duct of Cuvier [39], as we surmised this route of administration would directly expose ECs to 25HC. 25HC injections alone did not increase ICH occurrence in untreated larvae, however, in ATV-incubated larvae we observed a non-significant increase in ICH frequency (Fig. 6C). To assess the extent of cerebral bleeding, we next evaluated brain haematoma area in the same animals, showing that in ATV treated embryos, 25HC induced a significant increase in bleed area (Fig. 6D). As suggested by our *in vitro* experiments, this zebrafish ICH model demonstrates that 25HC and ATV interact and exacerbate neurovascular instability.

We then evaluated whether the ATV and 25HC interaction involved regulation of cholesterol metabolism. ATV incubation increased the expression of *hmgcrb*, a feedback response induced through SREBP2 activation [40], and 25HC co-incubation inhibited this process (Fig. 6E). This suggested that 25HC increased the sensitivity to ATV by decreasing HMGCR levels. To confirm whether the 25HC phenotype was dependent on ATV inhibition of HMGCR, we repeated the experiment in an alternative ICH zebrafish model. The homozygous *bbh* zebrafish mutant expresses a hypomorphic mutation in the *βpix* gene which leads to dysfunctional neuroendothelium, resulting in a comparable ICH phenotype to the ATV model independently of HMGCR activity [41]. 25HC injections in *bbh* larvae caused no differences in haematoma size (Fig. 6F). This demonstrated that 25HC effects on neurovascular stability are seemingly dependent on HMGCR inhibition. We then evaluated whether the 25HC effect was dependent on SREBP2 inhibition. For this we compared 25HC to another oxysterol, 4β-hydroxycholesterol (4βHC), which shares a similar structure (Fig. 6G) but has no effect on SREBP2 activity [16]. This was corroborated by *hmgcrb* expression in WT zebrafish larvae, which was significantly inhibited by 25HC incubation but not by 4βHC (Fig. 6H). When both oxysterols were injected alongside ATV incubation, only 25HC increased haematoma area in WT zebrafish larvae (Fig. 6I). These results revealed that 25HC increases the risk of ATV-induced ICH by inhibiting expression of SREBP2 targets, including the ATV target *hmgcrb*.

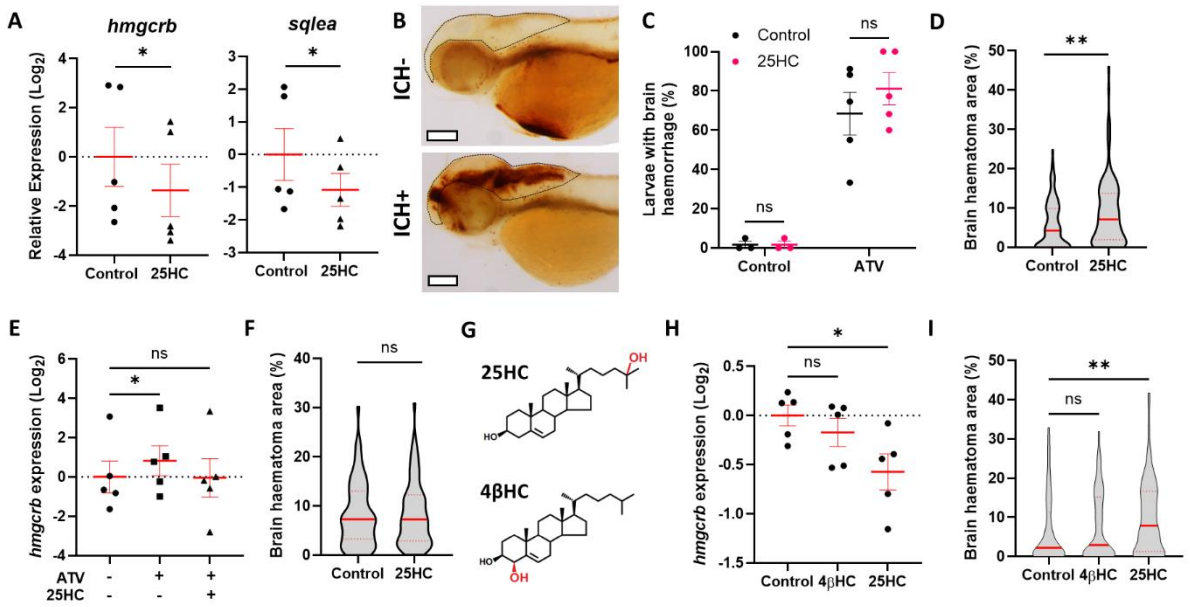

Figure 6. 25HC worsens brain haemorrhage expansion in statin-induced ICH zebrafish model. A *hmgcrb* and *sqlea* expression in 2 days post-fertilization (dpf) WT zebrafish larvae incubated with 25HC (25 µM, 24 h). **B-D** WT larvae were incubated in ATV (1 µM) at 28 hours post-fertilisation (hpf) and intravenously injected with 25HC (1 nl, 5 µM) at 32-36 hpf. Next day larvae were stained with O-dianisidine. Representative images of larvae without (ICH-) and with brain haemorrhage (ICH+) (**B**), ICH+ frequency per experiment (**C**) and brain haematoma area per larvae (**D**) were quantified (n=128 embryos, 5 independent experiments). Dotted lines indicate brain area. Scale bars 150 µm. **E** *hmgcrb* expression in 2 dpf WT larvae incubated with 25HC (25 µM) and ATV (1 µM) for 24 h. **F** *bbh* zebrafish larvae were injected with 25HC (1 nl, 5 µM) at 32-36 hpf. After 24 h larvae were stained with O-dianisidine and brain haematoma area was quantified (n=69-82 embryos, 3 independent experiments). **G** Comparison of 25HC and 4βHC structures. **H** Expression of *hmgcrb* in 2 dpf WT larvae incubated with 4βHC or 25HC (25 µM, 24h). **I** WT larvae were incubated in ATV (1 µM) at 28 hpf and injected with 4βHC or 25HC (1 nl, 2.5 µM) at 32-36 hpf. Next day larvae were stained with O-dianisidine and haematoma area was quantified (n=87-93 embryos, 3 independent experiments). Data are mean ± S.E.M (**A**, **C**, **E**, **H**) or median ± quartiles (**D**, **F**, **I**). *, $p < 0.05$; **, $p < 0.01$; ns, nonsignificant, determined by paired t-test (**A**), randomized block two-way ANOVA with Sidak's post-hoc test compared to control (**C**), Mann-Whitney test (**D**, **F**), randomized block one-way ANOVA with Dunnet's post-hoc test compared to control (**E**, **H**), or Kruskal-Wallis test with Dunn's post-hoc test compared to control (**I**).

Discussion

Here, we propose the CH25H/25HC pathway is an important component of brain EC dysfunction associated to infection and cholesterol dysregulation. Our findings in zebrafish larvae and human foetal samples suggest that CH25H is upregulated in viral-associated brain haemorrhages. CH25H upregulation may regulate brain vascular function, as we show that its product 25HC can induce brain EC dysfunction *in vitro* and in zebrafish ICH models. These results agree with previous observations on the regulation of vascular pathologies by the CH25H/25HC pathway. CH25H has been associated to endothelial inflammation in atherosclerosis, EAE and lung injury [18-20]. While these previous studies have primarily associated the CH25H/25HC pathway to ER stress [20] or regulation of inflammatory pathways [18,19], our data highlight cholesterol metabolism regulation as a key process controlling brain endothelial function.

We provide insight into how 25HC can dysregulate cholesterol metabolism and function of brain ECs using hCMEC/D3 cells. Notably, cholesterol supplementation rescued 25HC-induced dysfunction, while co-treatment with ATV and 25HC exacerbated dysfunction in hCMEC/D3 cells and a zebrafish model. Our results corroborate earlier reports indicating that cholesterol homeostasis is important for EC function. Previous studies have shown that dysregulation of cholesterol synthesis or disruption of cholesterol transport results in compromised angiogenesis and barrier function [29,30,42]. To the best of our knowledge, no other similar observations have been made specifically in human brain ECs to date. In our study, 25HC disrupted hCMEC/D3 barrier function while increasing VE-cadherin levels in cell junctions. Interestingly, a previous study reported the opposite, an increase in cholesterol synthesis associated with a reduction in VE-cadherin cell junction levels, which also resulted in similar disruption of EC barrier function [30]. These data suggest that VE-cadherin localization in cell junctions has an inverse association with cholesterol synthesis, while perturbation in cholesterol homeostasis, in either direction, leads to dysfunction of VE-cadherin cell-cell junctions. This is consistent with a previous report demonstrating that VE-cadherin function is sensitive to both increases and decreases in cholesterol levels [36].

In addition to the effects observed on VE-cadherin function, other cholesterol-modulated mechanisms may be involved in 25HC regulation of endothelial function. Dysregulation of the cholesterol synthesis pathway affects processes dependent on intermediate metabolites, such as prenylation, which relies on isoprenoids produced by HMGCR [43]. In our zebrafish model, the mechanisms of statin-induced ICH have been linked to decreased prenylation of endothelial Rho GTPases [21]. Decreased prenylation has been proposed as another antiviral mechanism for 25HC [44], therefore it is possible that 25HC treatment could also lead to defective prenylation in our *in vitro* and zebrafish models. Furthermore, other mechanisms related to shear stress response could be relevant to our zebrafish model. We report a decrease in accessible cholesterol in the plasma membrane of brain ECs, which could modulate cholesterol-dependent EC signalling in shear stress response [45,46]. A previous study also reported that 25HC can impair vasodilation of murine aortic rings by disrupting nitric oxide signalling [47]. Further studies are required to determine which other cholesterol-dependent processes are affected in brain ECs by 25HC.

While we report the expression of CH25H in human foetal brain tissue, we used exogenous 25HC to study the effects of the pathway in our *in vitro* and zebrafish models. Future investigations should assess the role of CH25H expression in brain vascular cell function. In response to inflammation, CH25H is upregulated and 25HC levels increase within the brain, as observed in models involving lipopolysaccharide (LPS) challenge [48] and tauopathy neurodegeneration [49]. CH25H is upregulated in microglia [49,50], and secretion of 25HC from LPS-stimulated microglia has been observed *in vitro* [50,51]. It is plausible that microglia-derived 25HC could modulate neurovascular function, similar to effects

reported in atherosclerosis where macrophage-derived 25HC regulates vascular inflammation [18]. Alternatively, endothelial intrinsic CH25H expression could also regulate neurovascular function, as CH25H upregulation has been detected in brain ECs in response to brain inflammation [19,52]. Cell-specific deletion has demonstrated a role of endothelial CH25H in EAE progression and cancer-associated angiogenesis [19,53], suggesting roles of endothelial CH25H beyond antimicrobial defence.

We report the upregulation of CH25H in SARS-CoV2-associated brain haemorrhages during early development in zebrafish and humans. Our results suggest that haemorrhages may occur due to an antiviral response rather than local infection, as spike protein injections in zebrafish larvae is a non-infectious model and no correlation between bleed score and cortical spike protein levels was found in human foetal samples. Indeed, maternal immune activation has been reported to lead to neurovascular developmental defects [54], including brain haemorrhages [55]. The effects of antiviral signalling in the developing brain can also be observed in monogenic conditions such as the type I interferonopathies. For example, early post-natal brain haemorrhages have been described for the Aicardi-Goutières syndrome 5 [56] caused by recessive mutations in the viral restriction factor SAMHD1, which we have previously modelled in zebrafish larvae [22,57]. The mechanisms involving immune activation and neurovascular dysfunction in the developing brain may differ from the mechanisms involved in adult ICH events. Most of the SARS-CoV-2-associated human foetal brain haemorrhagic cases previously reported occurred between 12 and 14 weeks post-conception [7]. This is a critical time window in neurovascular development where an increase of endothelial junction proteins has been reported [58,59]. Similarly, in the zebrafish ICH models included in this study, the bleeding occurs between 2-3 dpf [21,23,41], coinciding with brain angiogenesis and barrier function development [60]. Therefore, it is possible that an antiviral response may affect critical steps of brain vascular development that later leads to a vulnerability to vessel rupture.

Given that viral infections and hypocholesterolaemia are risk factors for ICH, further studies should explore whether the CH25H/25HC pathway is relevant for adult ICH. Models of infection-triggered brain haemorrhages in mammals are required for a better understanding of such a process. Spontaneous brain haemorrhages have been reported in adult mice following Japanese encephalitis virus and dengue infections [61,62]. However, these infections are associated with strong encephalitis or vasculitis phenotypes and may not resemble the milder clinical cases that report fever or flu symptoms as trigger factors of ICH [8]. It is possible that mild viral infections only trigger brain vessel rupture in combination with other risk factors and/or co-morbidities. Spontaneous murine ICH models involving hypertension or cerebral amyloid angiopathy [63] could be useful to evaluate this hypothesis. Murine models of LPS-induced inflammation have also reported spontaneous microbleeds [64,65]. As bacterial infection is also a risk factor for ICH [66], this could be an appropriate model to study the role of CH25H in infection-associated ICH. These models could also be useful to evaluate whether infection and the CH25H/25HC pathway regulate not only cellular cholesterol but also cholesterol at a physiological level.

In conclusion, we have reported the upregulation of CH25H in viral-associated developmental brain haemorrhages in a zebrafish model and in human foetal brain samples. Using *in vitro* and zebrafish models we have demonstrated that 25HC dysregulates brain EC function in a cholesterol metabolism-dependent manner. Our results highlight a novel association between the CH25H/25HC pathway, cholesterol dysregulation and brain EC dysfunction.

Methods

Zebrafish husbandry

Adult zebrafish husbandry was approved by The University of Manchester Animal Welfare and Ethical Review Board, and all experiments were performed per U.K Home Office regulations (PPL: PP1968962). The zebrafish used in this study were raised and maintained at The University of Manchester Biological Services Unit, under standard conditions, with adults housed in mixed-sex tanks with a recirculating water supply maintained at 28°C under a 14/10 hour light/dark cycle, as previously described [67]. Wild type AB, double transgenic Tg(fli1a:GFP)^{y1} / (gata1a:DsRed)^{sd2} [68,69] and βpix mutant *bbh* (*bbh*^{m292}) [41] adult zebrafish lines were used. Fertilized eggs were collected following natural spawning and incubated at 28 °C in fresh E3 medium, except embryos injected with SARS-CoV-2 spike protein which were kept at 26 °C until 48 hours post-fertilization (hpf) to delay development. The embryos were staged according to standard guidelines [70]. After termination of the experiment, all embryos were killed before protected status (5 dpf) using a lethal dose (4%) of Tricaine Methanesulfonate (MS222) and freezing at -20 °C.

SARS-CoV-2 spike protein zebrafish larvae ICH model

Tg(fli1a:GFP)^{y1} / (gata1a:DsRed)^{sd2} larvae were kept at 26 °C, dechorionated at 24 hpf and incubated with 0.3% N-phenylthiourea (PTU; Sigma-Aldrich) to inhibit melanogenesis. At 48 hpf, larvae were anaesthetized with MS222 (0.02%) and injected in the hindbrain with 2 nl of SARS-CoV-2 spike S1 protein (0.25 mg/ml) (SinoBiologicals, 40591-V08H3, molecular weight of 116 kDa) or BSA (0.43 mg/ml) (Sigma-Aldrich, molecular weight of 66.4 kDa) in PBS supplemented with phenol red 0.05%. Following hindbrain injections, larvae were kept at 28 °C and brain haemorrhages were detected and imaged *in vivo* using a Leica M165FC light stereo microscope with DFC7000T camera and processed using LASX software (version 3.3.3.16958). Images were analysed using ImageJ (version 1.54f), brain area (excluding the eyes) was manually selected and then threshold tool was used identically on all conditions to quantify gata1a positive brain area. Injections and manual selection of brain area were conducted blind to treatment.

Human foetal cortical samples

Human foetal tissues were obtained from the Human Development Biology Resource (HDBR), provided by the Joint MRC/Wellcome Trust (grant #MR/R006237/1) (www.hdbr.org). The HDBR provided fresh tissue from fetuses aged 9-21 post-conception weeks (pcw). Brains were fixed for at least 24 hours at 4°C in 4% (wt/vol) paraformaldehyde (PFA) in 120 mM phosphate buffer (pH 7.4). Brain cortexes were then sucrose-treated (15 and 30% sucrose solution sequentially for 24 h each), OCT-embedded, and then 20 µm thick sections were cut using a cryostat, as previously described [7].

Staining of human foetal samples

To visualise microbleeds, slides were stained with a haematoxylin and eosin (H&E) standard protocol and mounted with DPX mounting medium. For CH25H immunohistochemistry, antigen retrieval was performed by placing slides in 97.5 °C water bath in Tris-EDTA (pH 9.0) for 20 min. Non-specific binding was blocked with PBS with 5% goat serum, 0.3% Triton X-100 and 0.1% Tween for 1 h. CH25H antibody (Aviva system biology, OABF01697) was diluted at 1:2000 blocking solution and incubated on slide overnight at 4 °C. Slides then were incubated with biotinylated goat anti-rabit secondary antibody (BA-1000, Vector Laboratories) diluted in TBST buffer (tris-buffered saline with 0.1% tween and 0.1% BSA) at 1:400 for 90 min at RT. Slides then were stained with alkaline phosphatase ABC-AP Kit (AK-5000, Vector Laboratories), following manufacturer instructions. Finally, slides were counterstained with

haematoxylin and mounted with DPX. Slides were imaged using a 3D Histech Pannoramic 250 Flash Slide Scanner.

Images were analysed using the software QuPath (version 0.5.0). Bleed and total brain areas were manually selected, and CH25H+ cells were selected using a custom script. To evaluate CH25H+ cell distribution, representative regions of tissue were exported as tiled tiffs using CaseViewer (3Dhistech) and spatial coordinates of manually selected bleed cores and CH25H+ cells were measured using the software ImageJ.

Cell culture

The immortalised human cerebral microvascular endothelial cell line hCMEC/D3 cells (Merck) were cultured in endothelial cell growth medium MV (Promocell, C-22020) and PenStrep (100 units/ml penicillin and 100 µg/ml streptomycin) at 37 °C in a humidified atmosphere containing 5% CO2. Flask, plates and well inserts were pre-coated with rat tail collagen type I (Merck, UK), (1:100 in PBS) at 37 °C for 1 h, before hCMEC/D3 seeding. Cells were passaged at 100% confluency using Trypsin-EDTA solution (Sigma) and were used in experiments until passage 15.

hCMEC/D3 cells were seeded at a density of 71,000 cells/cm^2 overnight in all assays, with the exception of permeability and scratch assays (specific cell density stated in their subsections). Cells then were treated with 25HC (Sigma-Aldrich, H1015), Staurosporine (Cell guidance system, SM97), Mitomycin C (Roche, 10107409001), soluble cholesterol (Sigma-Aldrich, C4951) or ATV (Merck, SML3030), at concentrations and times stated in figure legends. When used as a carrier, control groups included ethanol or DMSO at the same concentration as treated groups.

Quantitative PCR

Total RNA was pooled groups of zebrafish larvae (n=30 larval heads, n=15 full larvae) or extracted from hCMEC/D3 cells seeded in 12 well/plates using a standard TRIzol (Invitrogen) method. Complementary DNA (cDNA) was synthesized from 800ng RNA as previously described (18). Quantitative PCR (qPCR) was performed on a StepOne Plus Real Time PCR machine (Applied Biosystems). cDNA samples were analysed using power SYBR green mastermix (Applied Biosystems) and primers (Thermo Fischer). Gene expression was normalized by geometric averaging of two internal control genes. Reference genes used were *hprt1* and *actb2* for zebrafish samples, and *HPRT1* and *18S* for human samples. A Taqman (Applied Biosystems) protocol and probes were used for *hmgcrb* and *sqlea* zebrafish genes, using *hprt1* as a reference gene. List of primers and Taqman probes in supplementary table 1.

Western blot

Western blot analysis was performed on hCMEC/D3 cell lysates using antibodies against full-length and cleaved caspase-3 (Abcam, ab32351, 1:500 dilution), VE-Cadherin (Cell Signalling, D87F2, 1:500 dilution) and β-Actin (Sigma-Aldrich, A3854, 1:10,000 dilution). Samples were run on 8% (Ve-Cadherin) or 12% (Caspase-3) SDS-polyacrylamide gels. Gels were transferred using a Trans-Blot® TurboTM Transfer System (Bio-Rad) at 25 V for 7 min before blocking PBST (PBS, 1% Tween 20) with 5% BSA in for 1 h at room temperature. Membranes were washed and incubated (4 °C) overnight in primary antibody in PBST with 0.1% BSA. Following this, membranes were washed and incubated with horseradish peroxidase–conjugated secondary antibodies (Dako) in PBST with 0.1% BSA for 1 h at room temperature. Finally, membranes were washed and incubated in Amersham Biosciences ECL Western Blotting Detection Reagent (GE Life Sciences) before exposure using a G:BOX gel doc system (Syngene). Densitometry was performed using Image J.

Streptolysin O (SLO) assay

hCMEC/D3 cells were seeded in 96 well/plates overnight and treated as previously stated. After cell treatments, media was changed to Opti-MEM reduced serum media (Thermo Fisher, 11058021) with To-Pro-3 0.5 µM (Thermo Fisher, T3605). SLO (Sigma-Aldrich, SAE0089) was activated with DTT 20 mM (30 min, 37 °C) before adding it to cells at 2 U/µl. Images were captured before SLO addition, and every 15 min after SLO addition using an IncuCyte ZOOM System (Essen Bioscience) with a ×20/0.61 S Plan Fluor objective. Excitation and emission wavelengths were 565–605 and 625–705 nm. 90 min after SLO addition, lysis solution (Promega, G1780) was added to capture an image with 100% permeability. Images were automatically analyzed using the IncuCyte software (Essenbio), using custom scripts which gave optimal detection for To-Pro-3 positive cells that ran identically on all conditions.

Fluorescein dextran permeability assay

hCMEC/D3 cells were seeded overnight at 50,000 cells/well in CellQart 24-well inserts with 0.4 µM pore size (Sterlitech, 9320412) and treated as previously stated. After cell treatments, media was changed to Opti-MEM reduced serum media, adding fluorescein dextran 70 kDa (FD70, 0.1 mg/ml) (Sigma-Aldrich, 46945) inside CellQart insert. 30 min later, fluorescence of media outside CellQart insert was measured using a Fluorstar reader (BMG Labtech), with excitation at 492 nm and emission at 520 nm.

Scratch assay

hCMEC/D3 cells were seeded in 6 well/plates overnight and pre-treated with 25HC for 24 h before re-seeding for scratch assay. hCMEC/D3 cells were seeded at 40,000 cells/well in 96 well ImageLock plates (Essen BioScience) and left to adhere for 4 h before scratch. During that time, cells were pre-treated with 25HC, mitomycin 5 µg/mL or soluble collagen for 1 or 2 h before scratch. Scratch wound injury was carried out using a 96-pin IncuCyte WoundMaker Tool (Essen BioScience). Cells were then washed twice with PBS and replaced with media. Phase contrast images were acquired at 2 h intervals for a period of 24 h using an Incucyte Zoom Live Cell Analysis system with a 4×/3.05 Plan Apo OFN25 objective. The 96-well Cell Migration Software Application Module (Essen BioScience) was used to quantify relative wound density, as previously described [32].

VE-cadherin immunofluorescence

hCMEC/D3 cells were seeded overnight on glass coverslips inside 24 well/plates. After treatments, cells were fixed in PFA 4% for 15 min and incubated in 5% BSA, PBST (PBS, 0.1% triton) for 30 min at RT. Coverslips were incubated with VE-Cadherin (Cell Signalling, D87F2) diluted at 1:200 and αTubuline (Sigma, T9026) diluted at 1:2000 for 1 h. Then coverslips were incubated with secondary Alexa-488 and -594 conjugated antibodies (Thermo Fisher) diluted at 1:500 in 0.1% BSA PBST for 1 h at 4 °C. Nuclei staining was performed with DAPI and after drying, coverslips were mounted with Prolong gold antifade reagent (Thermo Fischer). Images were collected on a Zeiss Axioimager.D2 upright microscope using a 20x / 0.5 EC Plan-neofluar objective and captured using a Coolsnap HQ2 camera (Photometrics) through Micromanager software v1.4.23. Images then were analysed for background removal with ImageJ, and then with Junction Mapper tool [37] to quantify VE-cadherin-based junction intensity. 4 images were taken for each replicate, 3-4 cells were manually selected (blinded to treatment) per image.

25HC zebrafish larvae ICH model

Zebrafish WT larvae were manually dechorionated and treated by immersion with ATV 1 µM (Merck) at 28 hpf. Control groups included HβCD (25HC carrier) in all experiments. For qPCR analysis, embryos

were treated by immersion with 25HC or 4βHC 25 µM, alongside carrier hydroxypropyl-β-cyclodextrin (HβCD) 0.11%, at the same time as ATV. For brain haemorrhage analysis, ATV-treated WT or *bbh* embryos were anaesthetised with MS222 (0.02%) between 32 and 36 hpf, and injected with 1 nl of 25HC or 4βHC (2.5 or 5 µM), HβCD 0.2%, phenol red 0.05% in PBS through the Duct of Cuvier [39]. To visualize bleeds, embryos were stained at 54 hpf using an o-dianisidine (Sigma) protocol, as previously described [21]. Stained embryos were mounted in 50% glycerol PBS and imaged in a Leica M165FC light stereo microscope with DFC7000T camera and processed using LASX software (version 3.3.3.16958). Images were analysed using ImageJ, brain area (excluding the eyes) was manually selected and then colour threshold tool was used identically on all conditions to quantify brain haemorrhage area. Injections and manual selections of brain area were conducted blind to treatment.

Data presentation and analysis

Data were presented as individual points with mean and S.E.M., except for individual zebrafish/cell imaging analyses represented as violin plots with median and quartiles. Experimental replicates (n) were defined as experiments performed on embryo clutches produced by different zebrafish adult pairs, individual zebrafish embryos, individual human donors, individual cells or different hCMEC/D3 passages. Experimental replicates were matched when measured several times (repeated measures ANOVA) or obtained from the same embryo clutches or hCMEC/D3 passages (randomized block ANOVA or paired t-test). Data were assessed for normal distribution using Shapiro-Wilk normality test. Parametric data were analysed using t-test or one-way ANOVA with Dunnett's post-hoc test. Non-parametric data were analysed using Mann-Whitney test or Kruskal-Wallis test with Dunn's post-hoc test. Two-factor data were analysed by two-way ANOVA with Sidak's post-hoc test or with Tukey's post-hoc test, time course data were analysed by two-way ANOVA with Dunnett's post-hoc test. Western blots are representative of 3-4 independent replicates. Statistical analysis was performed using GraphPad Prism (v10.2).

Acknowledgements

P.K. and V.S.T. were funded by Medical Research Council (MRC) grant MR/T03291X/1. C.B.L. and V.S.T. were funded by MRC grant MR/Y004183/1. S.E.W was funded by MRC Doctoral Training Programme studentship (MR/N013751/1). R.Z was funded by University of Manchester-China Scholarship Council Joint Scholarship. A.B. was funded by a 4 year British Heart Foundation PhD award (FS/4yPhD/F/22/34179). We thank the aquatics staff at the Biological Services Unit at The University of Manchester (UoM) for assistance with zebrafish care. We also thank the Bioimaging Core Facility at UoM.

Author Contributions

Conceptualisation: V.S.T., S.C. and P.R.K.

Methodology: V.S.T. and S.E.W.

Investigation: V.S.T., S.E.W., R.Z., A.B., F.H., A.E.K., N.L., M.M.

Resources: M.M. and K.R.L.

Visualisation: V.S.T.

Funding acquisition: C.B.L and P.R.K.

Supervision: V.S.T. and P.R.K.

Writing - original draft: V.S.T., C.B.L and P.R.K.

Writing - review and editing: all authors

Competing interests

The authors declare no competing interests.

Data availability

The data that support the findings of this study are available from the corresponding author upon reasonable request.

References

1 Collaborators, G. B. D. S. Global, regional, and national burden of stroke and its risk factors, 1990–2019: a systematic analysis for the Global Burden of Disease Study 2019. *The Lancet Neurology* **20**, 795-820 (2021). https://doi.org:10.1016/S1474-4422(21)00252-0

2 An, S. J., Kim, T. J. & Yoon, B. W. Epidemiology, Risk Factors, and Clinical Features of Intracerebral Hemorrhage: An Update. *J Stroke* **19**, 3-10 (2017). https://doi.org:10.5853/jos.2016.00864

3 Tseng, C. H., Muo, C. H., Hsu, C. Y. & Kao, C. H. Increased Risk of Intracerebral Hemorrhage Among Patients With Hepatitis C Virus Infection. *Medicine (Baltimore)* **94**, e2132 (2015). https://doi.org:10.1097/MD.0000000000002132

4 Hauer, L. *et al.* Cerebrovascular manifestations of herpes simplex virus infection of the central nervous system: a systematic review. *J Neuroinflammation* **16**, 19 (2019). https://doi.org:10.1186/s12974-019-1409-4

5 Nagel, M. A. & Gilden, D. Update on varicella zoster virus vasculopathy. *Curr Infect Dis Rep* **16**, 407 (2014). https://doi.org:10.1007/s11908-014-0407-z

6 Xu, E., Xie, Y. & Al-Aly, Z. Long-term neurologic outcomes of COVID-19. *Nat Med* **28**, 2406-2415 (2022). https://doi.org:10.1038/s41591-022-02001-z

7 Massimo, M. *et al.* Haemorrhage of human foetal cortex associated with SARS-CoV-2 infection. *Brain* **146**, 1175-1185 (2023). https://doi.org:10.1093/brain/awac372

8 van Etten, E. S. *et al.* Trigger Factors for Spontaneous Intracerebral Hemorrhage: A Case-Crossover Study. *Stroke*, STROKEAHA121036233 (2021). https://doi.org:10.1161/STROKEAHA.121.036233

9 Wang, X., Dong, Y., Qi, X., Huang, C. & Hou, L. Cholesterol levels and risk of hemorrhagic stroke: a systematic review and meta-analysis. *Stroke* **44**, 1833-1839 (2013). https://doi.org:10.1161/STROKEAHA.113.001326

10 Sun, L. *et al.* Causal associations of blood lipids with risk of ischemic stroke and intracerebral hemorrhage in Chinese adults. *Nat Med* **25**, 569-574 (2019). https://doi.org:10.1038/s41591-019-0366-x

11 Phuah, C. L. *et al.* Subacute decline in serum lipids precedes the occurrence of primary intracerebral hemorrhage. *Neurology* **86**, 2034-2041 (2016). https://doi.org:10.1212/WNL.0000000000002716

12 Betrisey, S. *et al.* Lipid-Lowering Therapy and Risk of Hemorrhagic Stroke: A Systematic Review and Meta-Analysis of Randomized Controlled Trials. *J Am Heart Assoc*, e030714 (2024). https://doi.org:10.1161/JAHA.123.030714

13 Mayerhofer, E. *et al.* Genetically predicted on-statin LDL response is associated with higher intracerebral haemorrhage risk. *Brain* **145**, 2677–2686 (2022). https://doi.org:10.1093/brain/awac186

14 Robertson, K. A. & Ghazal, P. Interferon Control of the Sterol Metabolic Network: Bidirectional Molecular Circuitry-Mediating Host Protection. *Front Immunol* **7**, 634 (2016). https://doi.org:10.3389/fimmu.2016.00634

15 Blanc, M. *et al.* The transcription factor STAT-1 couples macrophage synthesis of 25-Hydroxycholesterol to the interferon antiviral response. *Immunity* **38**, 106-118 (2013). https://doi.org:10.1016/j.immuni.2012.11.004

16 Heisler, D. B. *et al.* A concerted mechanism involving ACAT and SREBPs by which oxysterols deplete accessible cholesterol to restrict microbial infection. *eLife* **12:e83534** (2023). https://doi.org:10.7554/eLife.83534

17 Wang, S. *et al.* Cholesterol 25-Hydroxylase inhibits SARS-CoV-2 and other coronaviruses by depleting membrane cholesterol. *The EMBO Journal* **39** (2020). https://doi.org:10.15252/embj.2020106057

18 Canfrán-Duque, A. *et al.* Macrophage-Derived 25-Hydroxycholesterol Promotes Vascular Inflammation, Atherogenesis, and Lesion Remodeling. *Circulation* **147**, 388-408 (2023). https://doi.org:10.1161/CIRCULATIONAHA.122.059062
19 Ruiz, F. *et al.* Endothelial cell-derived oxysterol ablation attenuates experimental autoimmune encephalomyelitis. *EMBO reports* (2023). https://doi.org:10.15252/embr.202255328
20 Madenspacher, J. H. *et al.* 25-hydroxycholesterol exacerbates vascular leak during acute lung injury. *JCI Insight* (2023). https://doi.org:10.1172/jci.insight.155448
21 Eisa-Beygi, S., Hatch, G., Noble, S., Ekker, M. & Moon, T. W. The 3-hydroxy-3-methylglutaryl-CoA reductase (HMGCR) pathway regulates developmental cerebral-vascular stability via prenylation-dependent signalling pathway. *Dev Biol* **373**, 258-266 (2013). https://doi.org:10.1016/j.ydbio.2012.11.024
22 Withers, S. E. *et al.* Characterization of a mutant samhd1 zebrafish model implicates dysregulation of cholesterol biosynthesis in Aicardi-Goutières syndrome. *Front Immunol* **14**, 1100967 (2023). https://doi.org:10.3389/fimmu.2023.1100967
23 Tyrkalska, S. D. *et al.* Differential proinflammatory activities of Spike proteins of SARS-CoV-2 variants of concern. *Sci Adv* **8**, eabo0732 (2022). https://doi.org:10.1126/sciadv.abo0732
24 Pereiro, P. *et al.* Interferon-independent antiviral activity of 25-hydroxycholesterol in a teleost fish. *Antiviral Research* **145**, 146-159 (2017). https://doi.org:10.1016/j.antiviral.2017.08.003.
25 Liu, S.-Y. *et al.* Interferon-Inducible Cholesterol-25-Hydroxylase Broadly Inhibits Viral Entry by Production of 25-Hydroxycholesterol. *Immunity* **38**, 92-105 (2013). https://doi.org:10.1016/j.immuni.2012.11.005
26 Zhou, Q. D. *et al.* Interferon-mediated reprogramming of membrane cholesterol to evade bacterial toxins. *Nature Immunology* **21**, 746-755 (2020). https://doi.org:10.1038/s41590-020-0695-4
27 Saito, H. *et al.* Hydroxylation site-specific and production-dependent effects of endogenous oxysterols on cholesterol homeostasis: Implications for SREBP-2 and LXR. *J Biol Chem* **299**, 102733 (2023). https://doi.org:10.1016/j.jbc.2022.102733
28 Kennedy, M. A. *et al.* ABCG1 has a critical role in mediating cholesterol efflux to HDL and preventing cellular lipid accumulation. *Cell Metab* **1**, 121-131 (2005). https://doi.org:10.1016/j.cmet.2005.01.002
29 Zhou, R. H. *et al.* Vascular endothelial growth factor activation of sterol regulatory element binding protein: a potential role in angiogenesis. *Circ Res* **95**, 471-478 (2004). https://doi.org:10.1161/01.RES.0000139956.42923.4A
30 Tan, J. M. E. *et al.* The MARCH6-SQLE Axis Controls Endothelial Cholesterol Homeostasis and Angiogenic Sprouting. *Cell Reports* **32**, 107944 (2020). https://doi.org:10.1016/j.celrep.2020.107944
31 Afonso, P. V. *et al.* Alteration of Blood–Brain Barrier Integrity by Retroviral Infection. *PLoS Pathog* **4** (2008). https://doi.org:10.1371/journal.ppat.1000205
32 Thurgur, H., Penny, J. & Pinteaux, E. Endothelial cell activation by interleukin-1 and extracellular matrix laminin-10 occurs via the YAP signalling pathway. *J Neuroimmunol* **373**, 577993 (2022). https://doi.org:10.1016/j.jneuroim.2022.577993
33 Dejana, E. & Orsenigo, F. Endothelial adherens junctions at a glance. *J Cell Sci* **126**, 2545-2549 (2013). https://doi.org:10.1242/jcs.124529
34 Bentley, K. *et al.* The role of differential VE-cadherin dynamics in cell rearrangement during angiogenesis. *Nat Cell Biol* **16**, 309-321 (2014). https://doi.org:10.1038/ncb2926
35 Gentil-dit-Maurin, A. *et al.* Unraveling the distinct distributions of VE- and N-cadherins in endothelial cells: a key role for p120-catenin. *Exp Cell Res* **316**, 2587-2599 (2010). https://doi.org:10.1016/j.yexcr.2010.06.015
36 Baumgartner, W., Weth, A., Gutberlet, J., Harms, G. & Groschner, K. Localization of VE-cadherin in plasmalemmal cholesterol rich microdomains and the effects of cholesterol

depletion on VE-cadherin mediated cell–cell adhesion. *Biochim. Biophys. Acta* **1841**, 1725-1732 (2014). https://doi.org:10.1016/j.bbalip.2014.08.016
37 Brezovjakova, H. *et al.* Junction Mapper is a novel computer vision tool to decipher cell-cell contact phenotypes. *Elife* **8** (2019). https://doi.org:10.7554/eLife.45413
38 Li, S. *et al.* Discovery of a ROCK inhibitor, FPND, which prevents cerebral hemorrhage through maintaining vascular integrity by interference with VE-cadherin. *Cell Death Discovery* **3**, 17051-17011 (2017). https://doi.org:10.1038/cddiscovery.2017.51
39 Benard, E. *et al.* Infection of Zebrafish Embryos with Intracellular Bacterial Pathogens. *J. Vis. Exp.* **61** (2012). https://doi.org:10.3791/3781
40 Gobel, A., Breining, D., Rauner, M., Hofbauer, L. C. & Rachner, T. D. Induction of 3-hydroxy-3-methylglutaryl-CoA reductase mediates statin resistance in breast cancer cells. *Cell Death Dis* **10**, 91 (2019). https://doi.org:10.1038/s41419-019-1322-x
41 Liu, J. *et al.* A βPix–Pak2a signaling pathway regulates cerebral vascular stability in zebrafish. *PNAS* **104**, 13990-13995 (2007). https://doi.org:10.1073/pnas.0700825104
42 Koponen, A. *et al.* ORP2, a cholesterol transporter, regulates angiogenic signaling in endothelial cells. *FASEB J* **34**, 14671-14694 (2020). https://doi.org:10.1096/fj.202000202R
43 Zhang, F. L. & Casey, P. J. Protein prenylation: molecular mechanisms and functional consequences. *Annu Rev Biochem* **65**, 241-269 (1996). https://doi.org:10.1146/annurev.bi.65.070196.001325
44 Li, B. *et al.* 25-hydroxycholesterol inhibits human papillomavirus infection in cervical epithelial cells by perturbing cytoskeletal remodeling. *J Med Virol* **95**, e28834 (2023). https://doi.org:10.1002/jmv.28834
45 Park, H. *et al.* Plasma membrane cholesterol is a key molecule in shear stress-dependent activation of extracellular signal-regulated kinase. *J Biol Chem* **273**, 32304-32311 (1998). https://doi.org:10.1074/jbc.273.48.32304
46 Yamamoto, K., Nogimori, Y., Imamura, H. & Ando, J. Shear stress activates mitochondrial oxidative phosphorylation by reducing plasma membrane cholesterol in vascular endothelial cells. *Proc Natl Acad Sci U S A* **117**, 33660-33667 (2020). https://doi.org:10.1073/pnas.2014029117
47 Ou, Z. J. *et al.* 25-Hydroxycholesterol impairs endothelial function and vasodilation by uncoupling and inhibiting endothelial nitric oxide synthase. *Am J Physiol Endocrinol Metab* **311**, E781-E790 (2016). https://doi.org:10.1152/ajpendo.00218.2016
48 Waltl, S. *et al.* 25-Hydroxycholesterol regulates cholesterol homeostasis in the murine CATH.a neuronal cell line. *Neurosci Lett* **539**, 16-21 (2013). https://doi.org:10.1016/j.neulet.2013.01.014
49 Toral-Rios, D. *et al.* Cholesterol 25-hydroxylase mediates neuroinflammation and neurodegeneration in a mouse model of tauopathy. *J Exp Med* **221** (2024). https://doi.org:10.1084/jem.20232000
50 Cashikar, A. G. *et al.* Regulation of astrocyte lipid metabolism and ApoE secretion by the microglial oxysterol, 25-hydroxycholesterol. *J Lipid Res* **64**, 100350 (2023). https://doi.org:10.1016/j.jlr.2023.100350
51 Wong, M. Y. *et al.* 25-Hydroxycholesterol amplifies microglial IL-1β production in an apoE isoform-dependent manner. *Journal of Neuroinflammation* **17** (2020). https://doi.org:10.1186/s12974-020-01869-3
52 Chen, M. B. *et al.* Brain Endothelial Cells Are Exquisite Sensors of Age-Related Circulatory Cues. *Cell Rep* **30**, 4418-4432 e4414 (2020). https://doi.org:10.1016/j.celrep.2020.03.012
53 Lu, Z. *et al.* Regulation of intercellular biomolecule transfer–driven tumor angiogenesis and responses to anticancer therapies. *Journal of Clinical Investigation* **131** (2021). https://doi.org:10.1172/jci144225

54 Rasile, M., Lauranzano, E., Mirabella, F. & Matteoli, M. Neurological consequences of neurovascular unit and brain vasculature damages: potential risks for pregnancy infections and COVID-19-babies. *FEBS J* **289**, 3374-3392 (2022). https://doi.org:10.1111/febs.16020
55 Rasile, M. *et al.* Maternal immune activation leads to defective brain-blood vessels and intracerebral hemorrhages in male offspring. *EMBO J* **41**, e111192 (2022). https://doi.org:10.15252/embj.2022111192
56 Ramesh, V. *et al.* Intracerebral large artery disease in Aicardi-Goutieres syndrome implicates SAMHD1 in vascular homeostasis. *Dev Med Child Neurol* **52**, 725-732 (2010). https://doi.org:10.1111/j.1469-8749.2010.03727.x
57 Kasher, P. R. *et al.* Characterization of samhd1 morphant zebrafish recapitulates features of the human type I interferonopathy Aicardi-Goutieres syndrome. *J Immunol* **194**, 2819-2825 (2015). https://doi.org:10.4049/jimmunol.1403157
58 Virgintino, D. *et al.* Immunolocalization of tight junction proteins in the adult and developing human brain. *Histochem Cell Biol* **122**, 51-59 (2004). https://doi.org:10.1007/s00418-004-0665-1
59 Andrews, A. M. *et al.* Characterization of human fetal brain endothelial cells reveals barrier properties suitable for in vitro modeling of the BBB with syngenic co-cultures. *J Cereb Blood Flow Metab* **38**, 888-903 (2018). https://doi.org:10.1177/0271678X17708690
60 Quinonez-Silvero, C., Hubner, K. & Herzog, W. Development of the brain vasculature and the blood-brain barrier in zebrafish. *Dev Biol* **457**, 181-190 (2020). https://doi.org:10.1016/j.ydbio.2019.03.005
61 Tripathi, A., Banerjee, A. & Vrati, S. Development and characterization of an animal model of Japanese encephalitis virus infection in adolescent C57BL/6 mouse. *Dis Model Mech* **14** (2021). https://doi.org:10.1242/dmm.049176
62 Amaral, D. C. *et al.* Intracerebral infection with dengue-3 virus induces meningoencephalitis and behavioral changes that precede lethality in mice. *J Neuroinflammation* **8**, 23 (2011). https://doi.org:10.1186/1742-2094-8-23
63 Alharbi, B. M., Tso, M. K. & Macdonald, R. L. Animal models of spontaneous intracerebral hemorrhage. *Neurol Res* **38**, 448-455 (2016). https://doi.org:10.1080/01616412.2016.1144671
64 Sumbria, R. K. *et al.* A murine model of inflammation-induced cerebral microbleeds. *J Neuroinflammation* **13**, 218 (2016). https://doi.org:10.1186/s12974-016-0693-5
65 Zeng, J., Zhao, H., Liu, Z., Zhang, W. & Huang, Y. Lipopolysaccharide Induces Subacute Cerebral Microhemorrhages with Involvement of Nitric Oxide Synthase in Rats. *J Stroke Cerebrovasc Dis* **27**, 1905-1913 (2018). https://doi.org:10.1016/j.jstrokecerebrovasdis.2018.02.044
66 Boehme, A. K., Ranawat, P., Luna, J., Kamel, H. & Elkind, M. S. V. Risk of Acute Stroke After Hospitalization for Sepsis: A Case-Crossover Study. *Stroke* **48**, 574-580 (2017). https://doi.org:10.1161/STROKEAHA.116.016162
67 Westerfield, M. *The zebrafish book. a guide for the laboratory use of zebrafish (Danio rerio)*. 4th ed edn, (Univ. of Oregon Press, Eugene, 2000).
68 Traver, D. *et al.* Transplantation and in vivo imaging of multilineage engraftment in zebrafish bloodless mutants. *Nat Immunol* **4**, 1238-1246 (2003). https://doi.org:10.1038/ni1007
69 Delov, V., Muth-Kohne, E., Schafers, C. & Fenske, M. Transgenic fluorescent zebrafish Tg(fli1:EGFP)y(1) for the identification of vasotoxicity within the zFET. *Aquat Toxicol* **150**, 189-200 (2014). https://doi.org:10.1016/j.aquatox.2014.03.010
70 Kimmel, C. B., Ballard, W. W., Kimmel, S. R., Ullmann, B. & Schilling, T. F. Stages of embryonic development of the zebrafish. *Dev Dyn* **203**, 253-310 (1995). https://doi.org:10.1002/aja.1002030302

Supplementary table 1. qPCR primers and probes

Zebrafish primers		Sequence
hrpt1	forward	TTGCAGTAGCTTGTCGGTGT
hrpt1	reverse	CAGACGTTCAGTTCGGTCCA
actb2	forward	ATGGATGATGAAATTGCCGCAC
actb2	reverse	ACCATCACCAGAGTCCATCACG
ch25h	forward	CGGTGAATCCCATGTTGCTT
ch25h	reverse	AGCTCCTCCGTAAAGTCCAAAA
ch25hl1.1	forward	GTACTGCTGGCCTTCTCCAG
ch25hl1.1	reverse	GGCATAGGCATTACCACGTT
ch25hl1.2	forward	CGACTCAACCACTCAGAGACC
ch25hl1.2	reverse	AAGGTACGGCAGGACAAGAA
ch25hl2	forward	CAATGTACCTGGTGCTGGTG
ch25hl2	reverse	GCAGATGGTTGTACGTGGTG
ch25hl3	forward	TCTTCTCGGTGCCCTTCTTA
ch25hl3	reverse	AAACGCCAACCACGTATTTC

human primers		Sequence
HPRT1	forward	CAGGCGAACCTCTCGGCTTT
HPRT1	reverse	GGGTCGCCATAACGGAGCC
18S	forward	GTAACCCGTTGAACCCCATT
18S	reverse	CCATCCAATCGGTAGTAGCG
HMGCR	forward	GACGTGAACCTATGCTGGTCAG
HMGCR	reverse	GGTATCTGTTTCAGCCACTAAGG
SQLE	forward	CTCCAAGTTCAGGAAAAGCCTGG
SQLE	reverse	GAGAACTGGACTCGGGTTAGCT
ABCG1	forward	GAGGGATTTGGGTCTGAACTGC
ABCG1	reverse	TCTCACCAGCCGACTGTTCTGA

zebrafish Taqman probes	Sequence
hprt1	Dr03095135_m1
hmgcrb	Dr03128326_m1
sqlea	Dr03131215_g1